# Cerebellar contributions to a brainwide network for flexible behavior

Jessica L. Verpeut[1**], Silke Bergeler[1,2,3], Mikhail Kislin[1], F. William Townes[4], Ugne Klibaite[5], Zahra M. Dhanerawala[1], Austin Hoag[1], Caroline Jung[1], Junuk Lee[1], Thomas J. Pisano[1], Kelly M. Seagraves[1], Joshua W. Shaevitz[2,3], Samuel S.-H. Wang[1**]

[1]Neuroscience Institute, Washington Road, Princeton University, Princeton, NJ 08544 USA.
[2]Department of Physics, Princeton University, Princeton, NJ 08544 USA.
[3]Lewis-Sigler Institute for Integrative Genomics, Princeton University, Princeton, NJ 08544 USA.
[4]Department of Computer Science, Princeton University, Princeton, NJ 08544 USA.
[5]Department of Organismic and Evolutionary Biology, Harvard University, MA, 01451 USA.

**Corresponding authors

Correspondence: Samuel S.-H. Wang
Neuroscience Institute, Washington Road
Princeton University
Princeton, New Jersey 08544 USA
sswang@princeton.edu
+1 (609) 258-0388

Jessica Verpeut
Department of Psychology
Arizona State University
950 South McAllister Avenue
Tempe, Arizona 85281 USA
jverpeut@asu.edu
+1 (480) 727-5052

## Abstract

**The cerebellum regulates nonmotor behavior, but the routes by which it exerts its influence are not well characterized. Here we report a necessary role for posterior cerebellum in guiding flexible behavior, acting through a network of diencephalic and neocortical structures. After chemogenetic inhibition of Purkinje cells in lobule VI or crus I, high-throughput automated analysis of complex whole-body movement revealed deficiencies in adaptation across days to an open field environment. Neither perturbation affected gait, within-day open-field adaptation, or location preference. In a Y-maze task, mice could learn but were impaired in their ability to reverse their initial choice. To map targets of perturbation, we imaged c-Fos activation in cleared whole brains using light-sheet microscopy. Reversal learning activated diencephalic regions and associative neocortical regions. Distinctive subsets of structures were altered by perturbation of lobule VI (thalamus and habenula) and crus I (hypothalamus and prelimbic/orbital cortex), and both perturbations influenced anterior cingulate and infralimbic cortex. Taken together, these experiments reveal parts of a brainwide system for cerebellar influence to guide flexible learning.**

## Introduction

A recently appreciated contributor to flexible behavior is the cerebellum, a structure better known for its role in shaping movement and balance. Prominent anatomical pathways between cerebellum and neocortex suggest a role in higher-order processing [1–4]. Insult to the posterior cerebellum results in a clinical cognitive-affective syndrome that includes impairments in executive function, working memory, abstract reasoning, and emotional processing [5,6]. More severe outcomes arise from pediatric cerebellar insult, including a diagnosis of autism, a disorder

characterized by inflexibility to the point of emotional distress when routines are violated [7–12]. Taken together, these studies suggest that, like the neocortex, the cerebellum plays a necessary role in flexible behavior and cognitive processing.

Animal experiments have identified specific regions of the cerebellar cortex that support flexible behavior. In lobule VI, a midline posterior structure that is perturbed in autism spectrum disorder [13,14], inhibition of molecular layer interneurons alters reversal learning, perseverative or repetitive behavior, novelty-seeking, and social preference [15]. Disruption of right crus I, which is also perturbed in ASD, leads to deficits in social, repetitive, and flexible behaviors but does not affect gait [15,16]. Furthermore, inactivation of Purkinje cells in crus I reduces the ability to perform sensory evidence accumulation, a task in which Purkinje cells have been found to encode choices and accumulated evidence [17,18].

Lobule VI and crus I engage with the forebrain through bidirectional polysynaptic pathways [19]. Purkinje cells in the cerebellar cortex receive input from distal forebrain structures and send inhibitory output to cerebellar and vestibular nuclei, which in turn provide excitatory output to the rest of the brain forming the cerebral-thalamic-cerebellar circuit [20,21], [1–4]. Along these pathways, cerebellar cortex is organized into parasagittal microzones which project in distinctive patterns, so that lobule VI and crus I make different patterns of disynaptic connectivity with thalamic structures [22–24]. Trisynaptic tracing from these cerebellar regions leads to anterior cingulate, infralimbic, and somatosensory cortex [1–4,25].

To interrogate the contribution of the posterior cerebellum to flexible behavior, we monitored mouse behavior and mapped brain-wide patterns of activation after perturbing lobule VI and crus I. First, we chemogenetically perturbed neural activity reversibly in Purkinje cells, the principal output neurons of the cerebellar cortex. Second, we characterized freely-moving mouse behavior in granular detail using machine learning methods for automated tracking of body poses, movements, and actions. Third, we combined a Y-maze learning paradigm with c-Fos mapping to identify brain-wide substrates of reversal learning. Lastly, we studied expression of the activity-

dependent gene product c-Fos using tissue clearing techniques combined with light-sheet microscopy to map the whole brain without need for tissue sectioning. Together, these approaches provide a framework for characterizing how the cerebellum modulates flexible behavior.

## Results

*Experimental design to reversibly perturb Purkinje cells*

To probe the impact of cerebellar activity on flexible behavior and whole-brain activity, we chemogenetically inhibited Purkinje cells (PCs), which influence the rest of the brain via their projections to the deep cerebellar nuclei (DCN). The inhibitory DREADD (Designer Receptor Exclusively Activated by Designer Drugs) hM4Di was expressed in PCs using an adeno-associated virus (AAV) containing the hM4Di sequence under control of the L7 promoter. DREADD expression was robust and confined to PCs (**Figure 1A; Figure supplement 1A-C**). In slices, application of the DREADD agonist clozapine-N-oxide (CNO; 10 µM) reduced evoked action potential firing in hM4Di-positive PCs in slices (paired t-test, p = 0.0009) (**Figure 1B-D**), thus removing modulation of DCN neurons, which send excitatory output to the rest of the brain.

Posterior vermis (lobule VI and VII) and ansiform area (crus I and crus II) have been implicated in non-motor executive functions (**Figure 1E**) [15,26–28]. We injected virus into either lobule VI or crus I at postnatal day (PND) 56 and quantified mCherry-positive voxels (**Figure supplement 1D**). We then administered 1 mg/kg CNO on test days between PND 77 and PND 90 and tested animals on two paradigms for assessing flexible behavior: spontaneous behavior in an open-field arena, and reversal learning in a water Y-maze (**Table 1**). At different points of Y-maze training, we sacrificed mice to take tissue for whole-brain imaging of the activity-dependent immediate early gene c-Fos (**Figure 1F**).

*Lobule VI and crus I modulate multiday behavioral adaptation to an open field*

To measure the capacity of mice to adapt to a novel environment, we characterized spontaneous behavior in an open-field arena [29]. We video-recorded mouse behavior from beneath for 20 minutes over two days in order to track location and to allow automated tracking of body parts using the LEAP (LEAP Estimates Animal Pose) algorithm [30], in which a neural network was trained to track the positions of 18 joints (**Figure 2A, Figure 2B, movie supplement 1**).

Animals were recorded for 20 minutes on each of two days, after a dose of CNO on day 1 and a dose of vehicle on day 2 (**Figure 2A)**. Over successive days, control mice that did not receive AAV reduced their daily amount of locomotion (two-way mixed ANOVA $F(1,47) = 146$, $p < 0.001$) (**Figure 2A**). Disruption of lobule VI activity prevented this adaptation. Lobule VI-perturbed mice travelled significantly more on the second day ($d = 2.3$, one-way ANOVA $F(4,47) = 5.04$, $p = 0.002$, Dunnett post-hoc test $p < 0.001$) compared to the control group (**Figure 2A**. The total distance traveled on day 2 was not significantly different from the distance on day 1 in lobule VI perturbed mice, in contrast to a decrease for mice with a unilateral or bilateral disruption of crus I ($d = 2.6$, 2.4, and 1.4 for bilateral crus I, left crus I, and right crus I), or mice with a CNO injection without AAV ($d = 3.4$, repeated-measures ANOVA for each group, $p < 0.01$, Bonferroni correction) (**Figure 2A)**.

Perturbation of lobule VI or crus I did not change the fraction of time mice spent in the inner region of the open field arena compared to control animals on day 1. Right crus I-perturbed animals did spend a significantly larger fraction of time in the inner region of the open field arena on day 1 ($r = 0.6$, Kruskal-Wallis test chi-squared(4) = 9.52, $p = 0.049$, pairwise comparisons using Wilcoxon rank sum exact test $p = 0.02$, Benjamini-Hochberg correction) (**Figure supplement 2A**). None of the manipulations affected locomotory gait (**Figure supplement 2B**)

or spatial preferences in the arena such as locomotion in the periphery and grooming in corners (**Figure supplement 2C-D**).

To explore the structure of this altered behavior, we turned to automated pose analysis. We performed semi-supervised behavioral clustering on LEAP-tracked body-part locations to identify six clusters of body dynamics: slow exploration, grooming, fast exploration, rearing, turning walk, and locomotion. We used the clusters as behavioral states to generate an ethogram, arranged in order of increasing centroid speed (**Figure 2B**). Since mice spent the most time in locomotion, we further subdivided locomotion into three groups, slow, medium, and fast, based on centroid velocity (**Figure supplement 2C**).

The fractions of time spent in each of the eight behaviors was significantly different for lobule VI-perturbed mice compared to the control animals. More specifically, we found that compared with control animals, lobule VI disruption led to decreases in time spent in the rearing state on day 1 and increases in fast locomotion on day 2 (**Figure supplement 2D; Figure supplement 3A**). The increase in fast locomotion of lobule VI-perturbed mice compared to the control group on day 2 was a factor of 1.7, sufficient to account for the increased total distance traveled on day 2 compared to the other groups. Within each day's 20 minutes of observation, the probability of being in the fast locomotion state decayed over time. However, lobule VI-perturbed, bilateral crus I-perturbed, and right crus I-perturbed mice were more likely to perform fast locomotion just after the experiment started on day 2 compared to day 1, in contrast to our observations for the control group and left crus I perturbation (**Figure 2C**).

Complex adaptation was quantified by calculating the ratio of time spent in each state for day 2 and day 1. Overall, the adaptation ratio was closer to 1 for lobule VI-perturbed mice for most behavioral states, especially fast locomotion and slow exploration (**Figure 2D; Figure supplement 3B, Figure supplement 3D**). We next examined transition probabilities between behavioral states. In control animals, day 2 probabilities compared to day 1 showed higher

transition frequencies in the direction of less-active states (*i.e.,* above the diagonal of the matrix in **Figure supplement 2E**). This tendency was markedly reduced in lobule VI-treated animals. In crus-I perturbed mice, the same semi-supervised behavioral clustering analysis found subtle differences, in particular a right crus I-induced shift from fast-locomotion state to the slow-locomotion state starting on day 1 (**Figure 2D; Figure supplement 3A-C**). In summary, lobule VI-perturbed animals maintained similar within-day response patterns to the same environment despite impaired adaptation over two days of exposure.

*Cerebellar disruption of lobule VI or bilateral crus I impairs Y-maze reversal learning*

To test flexible learning, animals were trained to a water Y-maze (**Figure 3A**). After 1 day of habituation to the environment, an underwater platform was placed at the end of one Y-arm and the mice spent two days learning to find the platform through trial and error (acquisition days 2 and 3). On day 4, the platform was switched to the opposite arm for 4 sessions (reversal). On the fifth and final session on day 4, a barrier was placed blocking the originally learned side (forced reversal). On all days, correct choice was defined as an entrance to the correct arm and climbing onto the platform during the 40-second trial.

All DREADD-activated groups showed a similar time course of initial acquisition, showing no statistically detectable differences compared with controls (generalized linear mixed-effect model, GLMM, p=0.76; **Figure 3B**). Neither surgery by itself, nor the effects of administering vehicle-only, CNO-without-DREADD, or CNO-with-mCherry, affected distance swum, initial learning, or reversal-learning compared with untreated mice (**Figure supplement 4A-D**).

Lobule VI-perturbed mice and bilateral crus-I-perturbed mice were strongly impaired in reversal learning (**Figure 3C and Figure supplement 4E**; lobule VI compared to CNO-without-DREADD controls $p = 8.9*10^{-06}$, bilateral crus I $p = 0.04$). Performance on the forced-reversal session was also reduced (lobule VI, p = 0.0039) (**movie supplement 2**). In tests for lateralization

of crus I function [31], we found that neither left- ($p = 0.83$) or right- ($p = 0.10$) crus-I-perturbed mice showed impaired reversal (**Figure 3C**).

To probe behavioral patterns of this learning failure, we analyzed individual trials. Entrance into any arm N times, ending with a landing in the correct arm, was defined as an N-th choice trial. Even in the first reversal session, control mice (CNO only) typically found the platform in their first or second choice (85% of mice), eventually making the correct first choice in 71% of trials by the fourth session. In contrast, lobule-VI-perturbed mice made persistent errors even by the fourth session, making correct first choices on 16% of trials and correct second choices on 34% of trials (**Figure 3D and Figure supplement 4F**). In forced-reversal trials, lobule-VI-perturbed mice displayed a unique perseverative behavior of swimming back and forth between the divider and beginning of the maze instead of switching to the obvious open arm, resulting in animals failing to switch in 64% of forced-reversal trials (**movie supplement 2**). This perseveration was also observed in crus-I perturbed mice, whereby mice continued to swim to the previously correct arm and failed to switch in 47% of forced-reversal trials. (**Figure 3D, Figure supplement 4F**). In summary, mice typically learned the Y-maze by trying multiple arms until the platform was found, but perturbing the cerebellum resulted in persistent errors and a failure to reverse.

*Whole-brain c-Fos reveals lobule-specific behavior*

We next sought to identify brain-wide targets of cerebellar influence that could account for the observed perseverative and inflexible behavior. Brains were extracted at different points in the Y-maze learning and reversal paradigm to quantify expression of the activity-dependent immediate early gene c-Fos [32]. Brains were cleared using iDISCO+ [33] and immunostained for c-Fos and the mCherry fluorescent tag encoded by both DREADD and control AAVs (**movie supplement 3**). Samples were imaged for AlexaFluor-647 on a light-sheet microscope, aligned to the Princeton

Mouse Atlas [1–4,25], and analyzed for c-Fos positive cells using ClearMap [34] (**Figure 4A; movie supplement 3**). Using 122 chosen structures, a 3-D representation of the data was created for each brain using Neuroglancer, a Google WebGL-based viewer for volumetric data (**Figure 4A**) for analysis of c-Fos in single or combined regions (**Figure 4B**).

Within each paired comparison, brains from all control and treatment animals were processed as a single batch using the same tissue preparation and imaging conditions whenever possible. In the few cases where multiple batches were needed, we adjusted for confounding due to batch effects by including indicator variables as covariates in regression models. Analogous to genome-wide association studies, each brain region was analyzed independently and the results corrected *post hoc* to control the false discovery rate. For each region, the contrast between counts for the animals in the treatment group versus the control group was quantified using negative binomial regression with a log link function. To account for animal-specific variation in total counts, the log of total counts was included as an offset (**Figure 4C**).

To identify brain regions activated in the initial acquisition of Y-maze learning, we assayed c-Fos-positive cells immediately after 3 days of Y-maze ending on the last initial acquisition day (n=10 mice), using for baseline comparison animals that underwent habituation-only on the first day of Y-maze (n=10 mice; **Figure supplement 5** and **Figure supplement 6A**). Out of 122 regions, 33 regions showed increased activity and 6 regions showed decreased activity. We found activation in thalamus (1.4-fold) and in prelimbic (1.8-fold) and temporal association (1.65-fold) cortex. In the rest of the brain, we found some of the strongest associations in parabrachial nucleus (2.8-fold), basolateral, central, and cortical amygdalar nucleus (1.8, 1.7, and 1.7-fold), lateral habenula (2.3-fold), periaqueductal gray (2.1-fold), septohippocampal nucleus (2.9-fold), and lateral septal nucleus (2.6-fold) (**Figure supplement 5, Figure supplement 6A, Figure supplement 7A-B**). Overall, initial learning specifically activated a wide range of regions linked with associative and affective function.

We then assessed specific neural correlates of reversal learning by comparing brains on day 4 after one day of reversal learning (n=10 mice) with mice undergoing a third day of acquisition (n=8) (**Figure 4D, Figure 6, Figure Supplement 6B**). We found statistically significant activation throughout thalamus (2.7-fold), including polymodal regions (3.2-fold) as classified by Jones, sensory/motor regions (2.1-fold), and the reticular nucleus, which is modulatory (3.2-fold) [35,36]. Reversal learning was associated with decreases in the majority of neocortical regions, the largest change being a decrease in infralimbic cortex activity (0.56-fold). Additional activation was seen in medial and lateral habenula (15.6-fold and 7.6-fold), periaqueductal gray (1.9-fold), and parabrachial nucleus (1.6-fold) (**Figure 6, Figure supplement 7A-B**).

We next focused on the effects of lobule VI perturbation (n=10 mice) on reversal learning. Perturbation of lobule VI during reversal learning (**Figure 5A-C, Figure 6, Figure Supplement 6C, Figure supplement 7A-B**) resulted in a reduction in c-Fos activity throughout thalamus (overall 0.28-fold compared with unperturbed reversal learning). Increased activity was seen in somatomotor, somatosensory, anterior cingulate, and infralimbic cortex. Midbrain regions both increased (ventral tegmental area, lateral hypothalamus, midbrain raphe nuclei) and decreased (parastrial, medial and lateral habenula, and periaqueductal gray) in activity. Such widespread changes were not seen when giving CNO during an additional day of acquisition (**Figure 5D**).

We also tested the consequences of bilateral crus I perturbation on reversal learning (**Figure 6A : left**). Bilateral perturbation of crus I during reversal learning did not lead to statistically significant changes in thalamic activity compared with unperturbed reversal learning. However, changes were seen in the neocortex, both increases (anterior cingulate, prelimbic, infralimbic, and orbital) and decreases (auditory, visual, posterior parietal, and temporal). Increases were also seen in parastrial nucleus and hypothalamus (lateral and preoptic). These changes were not seen after unilateral perturbation of crus I (**Figure supplement 5**).

Many effects of lobule VI and crus I perturbation went in the opposite direction as the reversal-versus-acquisition condition. Of the 61 regions showing changed activity in reversal

learning, 47 were changed in the opposite direction by lobule VI perturbation, and 27 changed by crus I bilateral perturbation. Opposite-direction changes encompassed the majority of thalamic regions and lateral and medial habenula, as well as selected regions in telencephalon (anterior cingulate, infralimbic) and mesencephalon (periaqueductal gray, pretectal regions) with a lobule VI perturbation (**Figure 6A)**. The overall pattern of cell ratios was strongly correlated for lobule VI (correlation of log-cell-ratios by Pearson's r = -0.78) (**Figure 6C)**, and less correlated for crus I (Pearson's r =-0.29) **(Figure 6B)**. Thus, lobule VI perturbation reversed activation patterns in most regions that were activated by reversal learning, while crus I perturbation had effects that were limited to neocortical and hypothalamic regions.

## Discussion

We found that intact cerebellar function in lobule VI and crus I was necessary for two acquired flexible behaviors, adaptation to an open field and choice reversal in a swimming Y-maze. In both behavioral paradigms, silencing of Purkinje cells led to deficits that became apparent over a period of several days, and in the case of Y-maze was marked by repetitive action even in the face of reinforcement. Y-maze choice reversal recruited activity in a diencephalon-centered group of regions, most of which were reversed by inhibition of Purkinje cells in lobule VI; and in prefrontal and hypothalamic regions, which were reversed by inhibition of either lobule VI or crus I. Taken together, these studies comprise a demonstration of cerebellar perturbation leading to specific alterations in whole-brain activity and nonmotor function.

Identification of effects on flexible behavior required us to distinguish them from changes in the coordination of movement. Our pose analysis [29] enabled us to simultaneously analyze the detailed kinematics of limb movement and longer time-scale features of behavior. Such an analysis required a method that could track individual body parts, such as LEAP [30] or other approaches [37,38]; [39,40]. We did not find differences in gait or in spatial occupancy of the arena, suggesting that the chosen cerebellar perturbations affected the evolution of motor behaviors over

several days, but not the capacity to interact with the physical environment or generate locomotor behavior. These results are consistent with past work in which rodent gait was not altered by lobule-specific perturbation of posterior cerebellum [15,16], but was changed by cerebellum-wide disruption [29,41,42].

Flexible cognition, as examined by Y-maze reversal learning, was found to be strongly modulated by lobule VI and crus I. Mice demonstrated perseveration in this task by swimming repeatedly toward the previously learned arm before finding the platform in the third arm of the Y-maze, even when the incorrect arm was blocked. Perseverative behavior is a principal criterion for autism spectrum disorder [43–45]. Vermal lobules VI-VII are altered in their volume developmental trajectory in ASD children compared with the rest of cerebellum [13,14], suggesting a potential role for lobule VI in driving ASD-like outcomes. In the open field, lobule VI-perturbed mice demonstrated reduced adaptation by staying in a fast locomotive state on both days. Given the widespread disruption of thalamic activity caused by inhibiting lobule VI output, these behavioral deficits may arise from the disruption of sensory or polymodal processing, reducing the capacity of the forebrain to detect novelty or process its consequences.

We found that disruption of crus I altered both multiday adaptation to the open field and the ability to reverse learning in a swimming Y-maze. Crus I has been implicated in social processing both in mice and in humans with ASD [16,46] and crus I is engaged in the processing of sensory novelty in human studies [47,48]. Due to the spread of injections, crus II may be an additional route by which our experiments affected behavior. Taken together, our findings are in accordance with lobule-specific substrates for a number of deficits that arise in cerebellar cognitive-affective disorder [5,6,49].

The cerebellum influences the rest of the brain through polysynaptic paths through the deep and vestibular nuclei. By analyzing the immediate-early gene c-Fos, we found that reversal learning engaged midbrain, diencephalic, and neocortical regions associated with flexible behavior, and that this engagement was reversed by perturbation of lobule VI. Many of these

brain regions receive disynaptic paths from lobule VI and crus I, as demonstrated by transsynaptic tracing [1–4,25]. In the midbrain, the habenula, periaqueductal gray, and parabrachial nucleus are engaged during defensive, negative-reward, and decision-making behavior [50–53]. Finally, the infralimbic and anterior cingulate cortex are activated in effective decision making and reward-seeking [54–56]. Our observation that lobule VI and crus I inhibition affects activity in these regions during reversal learning suggests that cerebellar activity is necessary for the normal expression of a wide range of brain activity in the face of changing environmental valence.

Recent studies show that vermal and hemispheric regions project via the deep cerebellar nuclei to distinctive patterns of forebrain structures [57] [1–4]influencing thalamocortical nonmotor processing. Chemogenetic inhibition of lobule VI Purkinje cells led to broad decreases in thalamic activity as measured using c-Fos. A major target of cerebellar output, especially from lobule VI/VII, is the thalamic reticular nucleus [1–4,25], which is inhibitory and sends its outputs throughout the rest of the thalamus. Reticular nucleus paths have been suggested to have a gating effect on thalamocortical function [58] and are important for flexible behavior [59–62]. In addition, removal of Purkinje-cell inhibition in lobule VI might be expected to increase activity in thalamic polymodal nuclei via cerebellothalamic excitation, providing a means by which effects might differ across thalamic nuclei. The fastigial nucleus, which receives strong lobule VI input, has recently been shown to send output to brainstem targets subserving arousal and autonomic functions [571–4]. The widespread nature of lobule VI's functional targets supports the idea that the cerebellum acts as a powerful modulator of thalamocortical processing in situations that call for flexible behavior.

Chemogenetic inhibition of crus I Purkinje cells also led to changes in neocortical activity as measured using c-Fos. Crus I [1–4,25] projects to thalamus, both sensory/motor such as ventral posteromedial nucleus and polymodal such as lateral dorsal nucleus, and to hypothalamus, which like the thalamus is a diencephalic structure that projects monosynaptically to neocortex [63]. Transsynaptic paths from crus I project particularly densely to infralimbic, prelimbic, and orbital cortex, providing a substrate for our observed alterations in c-Fos expression.

Lobule VI perturbation changed thalamic c-Fos activation more than it changed neocortex, and crus I perturbation changed neocortex but not thalamus. One obvious explanation is that neocortex receives inputs from many nonthalamic sources, and indeed disjoint activation of thalamus and neocortex has been long known [64,65]. Mapping of c-Fos may also fail to capture all relevant changes. Expression of c-Fos depends in a complex and cell-type-dependent manner on activity [66]. Furthermore, c-Fos expression persists for many minutes, far longer than the timescale of synaptic chains of activation (<1 s). Thus, our results could have potentially arisen from later events including long-term consequences of failing to complete the task.

Lateralization of cerebellar function has previously been reported both in mice and in humans with ASD [16,46]. We observed some lateralization of effect for right crus I perturbation on open-field adaptation, but not Y-maze reversal. Left-right lateralization might be expected to be opposite to that of neocortex because ascending paths decussate on the way from deep nuclei to thalamus. However, when the ascending connection from cerebellar cortex is traced, ipsilateral and contralateral paths to nonmotor cortex are similar in strength [1–4,25], suggesting that any cerebellar lateralized function should either be weaker or differ from neocortex.

In summary, we have used chemogenetic inhibition of Purkinje cells to identify two cerebellar regions that influence multiday flexible behavior, lobule VI and crus I. Detailed characterization of c-Fos activation in Y-maze, including different stages of learning (habituation, acquisition/“nonreversal”, and reversal), revealed brainwide consequences of the task and focal perturbations. First, more challenging task conditions led to progressively more widespread regional activation. Second, cerebellar perturbation affected activity in regions that were activated under reversal learning, including thalamus by lobule VI and neocortex by crus I. Brain-wide c-Fos mapping serves as a screen analogous to the introduction of the Genome-Wide Association Study in 2002 [67]. Understanding the task-specific role for cerebellum in driving forebrain neural processing will require direct recording or high-time-resolution perturbation of the candidate regions we have identified.

## Methods

### Data and Code Availability

The dataset is available at Princeton data DOI: https://doi.org/10.34770/c9df-sc15. All experimental and analysis code is available here: https://github.com/PrincetonUniversity/OF-ymaze-cfos-analysis.

*Experimental Design*

To investigate the role of cerebellar lobule-specific roles in a flexible cognitive task, we targeted neural activity of Purkinje cells of mice using Designer Receptors Exclusively Activated by Designer Drugs (DREADDs). We delivered adeno-associated virus (AAV) with the sequence for the inhibitory DREADD hM4Di, which was fused to mCherry protein under a Ef1α promoter. This virus included a DIO component, which when combined with the L7-cre virus, expressed in the PC layer exclusively (**Figure 1A; Figure supplement 1A-C**). Mice used in this study were male C57BL/6J (The Jackson Laboratory, Bar Harbor, ME) and acclimated for at least 48 hours at the Princeton Neuroscience Institute vivarium prior to procedures. After a three-week recovery period, mice (PND 70) underwent behavioral testing starting with social behavior, then open field, and water Y-maze reversal for whole-brain c-Fos analysis (**Figure 1F**). Recently clozapine-N-oxide (CNO) has been found to convert back to the parent compound, Clozapine, in mice prior to crossing the blood-brain barrier. To reduce confounds in our experimental design, all mice received CNO during all behavioral tasks, as Clozapine may alter signaling of neuromodulators, notably dopamine and serotonin [68–70].

For DREADD experiments, lobules targeted were lobule VI (n = 20), bilateral crus I (n = 17), crus I right (n = 25), crus I left (n = 26), but as AAV can spread into neighboring lobules, mCherry fluorescence was recovered and quantified for the entire cerebellum. Controls included animals injected with AAV without DREADDs (CNO and mCherry, n = 17), CNO only (n = 25), Vehicle (DMSO and saline, n = 9), and untreated (n = 51). To understand if CNO or a lobule-specific perturbation altered Y-maze performance without reversal a subset of CNO only (n = 7)

and CNO and Lobule VI mice (n = 10) underwent 25 trials of a third day of acquisition. To understand learning in the y-maze, animals with 10 per group were sacrificed after habituation, acquisition day 1, and acquisition day 2 (total of 30 mice), see Table 1. All mice were housed in Optimice cages (Animal Care Systems, Centennial, CO) and received environmental enrichment, including paper nesting strips and one heat-dried virgin pulp cardboard hut (Shepherd Speciality Papers, Milford, NJ). Mice were fed PicoLab Rodent Diet food pellets (LabDiet, St. Louis, MO) and water was provided ad libitum. Cages were changed every two weeks and animals were housed in groups of 4-5 mice in reverse light cycle rooms to maximize normal nocturnal activity, as behavior testing occurred during the day. All experimental procedures were approved by the Princeton University Institutional Animal Care and Use Committee and in accordance with animal welfare guidelines of the National Institutes of Health.

*Animal preparation*

Mice underwent surgery similar to previous published procedures [15,71,72] at postnatal day 56. Briefly, animals were anesthetized with isofluorane (5% induction, 1-2% oxygen; 1 L/min) and mounted in a stereotaxic device (David Kopf Instrument, Tujunga, CA) for all surgeries. Temperature was monitored and automatically adjusted using PhysioSuite (Kent Scientific Corporation, Torrington, CT). Animals were prepared for surgery with an application or Puralube vet ointment (Pharmaderm Florham Park, NJ) to prevent corneal drying, the scalp was shaved and cleaned, and animals received osmotic diuretic drug 15% D-mannitol in DPBS (0.02ml/g; intraperitoneal, i.p.) and an anti-inflammatory drug, Rimadyl (5mg/kg Carprofen 50 mg/ml, Pfizer, Eurovet, in NaCL; every 24 hours for 2 days; subcutaneous, s.c.). A lateral skin incision was made over the lambdoid suture. Muscle was cut over the occipital bones first vertically than horizontally and as close to the bone as possible to allow for regrowth post-surgery and enough to expose lobule VI or crus I.  A small craniotomy was made over each lobule of interest for injection of inhibitory DREADD AAV1-Eflα-DIO-hM4D(Gi)-mCherry-WPRE-hGHpA (8.5 x 10^13;

PNI Vector Core, AAV-VC68) or control AAV8-Eflα-DIO-mCherry-WPRE-hGHpA (1 x 10^15; PNI Vector Core, AAV-VC139). To target Purkinje cells, both DREADD and control AAVs were mixed in a 1:1 ratio with AAV1-sL7-Cre-HA-WPRE-hGH-pA (2 x 10^14; PNI Vector Core, AAV-VC141). Confirmation of mCherry expression and Purkinje cell inhibition by DREADD activated by CNO was determined (**Figure 1B-C**). Virus was injected using borosilicate glass capillaries (World Precision Instrument, Sarasota FL) made using the Sutter Micropipette Puller (Model P-2000, Sutter Instrument Company) and bevelled at a 45 degree angle. To ensure viral spread ~600nl total of DREADD or control was injected per mouse, distributed at 3 separate depths (150, 250, 450 µm below the dura) and two locations per lobule. Craniotomy was sealed with a silicone elastomer adhesive (Kwik-Sil, World Precision Instrument, Sarasota, Fl) and skin was sutured. All mice were tested two weeks post-surgery at P70.

*Tissue processing and histology*

To examine mCherry fluorescence, the presence of DREADD virus, two mice were anesthetized with Euthasol (0.06 ml/30g, i.p.) and perfused with 4% paraformaldehyde (PFA). Brains were stored overnight at 4% PFA then placed in 20% sucrose in PBS overnight until sectioning at 50 µm. Sections were washed with PBS and incubated for 1 hr at room temperature in blocking buffer (10% normal donkey serum, 0.5% Triton in PBS) prior to an overnight incubation at 4℃in PBS buffer with 2% normal donkey serum, 0.4% Triton and the rabbit anti-RFP (600-401-379, Rockland Immunochemicals, Inc., Limerick, PA; 1:1000) primary antibody. The next day, sections were washed in PBS and incubated for 2 hr at room temperature in PBS buffer with 2% normal donkey serum, 0.4% Triton, and the donkey anti-Rabbit Alexa Fluor 647-conjugated secondary antibody (A-21449; Thermo Fisher Scientific, MA, USA, Invitrogen; 1:400).Tissue was mounted on glass slides with Prolong Diamond (ThermoFisher Scientific, MA, USA). A separate sample examined for the presence of the hemagglutinin tag present on the L7-cre plasmid using the same staining protocol with the additional primary antibody anti-HA (71-500,

ThermoFisher Scientific, MA, USA, 1:1000). Tissue was imaged with a Leica SP8 confocal laser-scanning microscope (Leica Microsystems, Germany) using 40x or 63x objectives (**Figure supplement 1 B-C**).

After animals completed the last Y-maze reversal session, animals were placed back in their home cage for 90 minutes. Then mice were anesthetized with Euthasol (0.06 ml/30g, i.p.) and perfused with 4% PFA for analysis of c-Fos and mCherry expression for DREADD recovery. All brains underwent the same iDISCO+ clearing protocol as previously described. [1–4,25] Briefly, after an overnight fix in 4% PFA, brains were rinsed in phosphate buffered saline (PBS) at room temperature (RT) for four 30 minute sessions. Immediately brains were dehydrated 1 hr at each ascending concentration of methanol (20, 40, 60, 80, 100, 100%) and placed overnight in 5% hydrogen peroxide and methanol at RT. The next day, brains were rehydrated for 1 hr at each descending concentration of methanol (100, 80, 60, 40, 20%) and lastly PBS. Samples were placed in detergent (0.2% Triton X-100 in PBS) for two 1 hr sessions then placed for two days in 20% Dimethyl sulfoxide (DMSO), 0.3 M glycine, 0.2% Triton X-100 in PBS at 37°C. Brains were blocked in 10% DMSO, 6% donkey serum, 0.2% Triton X-100 in PBS at 37°C for 3 days. Once at room temperature, samples were washed in PTwh (0.2% Tween-20, 10µg/ml heparin in PBS) and placed in primary solution of rabbit anti-Fos (226 003, Synaptic Systems,Goettingen, Germany, 1:1000) and rabbit anti-RFP (600-401-379, Rockland Immunochemicals, Inc., Limerick, PA; 1:450) for one week at 37°C. To recover EGFP for HSV injections, the chicken anti-GFP primary antibody (GFP-1020, Aves Labs Inc., Oregon, USA; 1:1000, [15,731–4]. Brains were washed in PTwH five times in increasing amounts of time (10, 15, 30, 60, 120 min) and then placed in secondary donkey anti-Rabbit Alexa Fluor 647-conjugated secondary antibody (A-21449; Thermo Fisher Scientific, MA, USA, Invitrogen; 1:200) for one week at 37°C. Brains were washed in PTwH five times in increasing amounts of time (10, 15, 30, 60, 120 min) then dehydrated 1 hr at each ascending concentration of methanol (20, 40, 60, 80, 100, 100%) until being placed in 66% DCM/33% methanol for 3 hrs at RT. Brains were cleared

with 100% dichloromethane (DCM) for two 15 min steps then placed in 100% benzyl ether (DBE). Brains were kept in fresh DBE prior to imaging and after for long-term storage. Tissue was imaged using a light-sheet microscope (Ultramicroscope II, LaVision Biotec., Bielefeld, Germany).

*Behavioral testing*

All behavior testing began at P70 and animals were tested in the following order: (1) open field, (2) water Y-maze. Animals were also tested for three-chamber social preference and novelty seeking [15] but showed no effects. For each experiment, animals were allowed to acclimate to the testing room for at least 60 minutes. During this time, animals receiving CNO (1 mg/kg, i.p.) or vehicle (1.5% dimethyl sulfoxide in saline, i.p.) were lightly anesthetized for injection and allowed at least 20 minutes of recovery prior to experiments. Animals performed Y-maze under low white light. For open field mice were recorded under red light as it was observed that mice would not enter the middle of the plexiglass arena under white light.

Open Field: Wild-type (n = 60), mice with a cerebellar perturbation (n = 10 per group), and mice with a Purkinje-cell specific tuberous sclerosis 1 gene mutation (L7Cre; $Tsc1^{flox/flox}$) (n = 9) [42,74] were placed in an open field arena measuring 45.72 x 45.72 cm (length x width) and 30.48 cm in height with a transparent polycarbonate floor, as previously described [29]. A Point Grey grayscale camera (12-bit grayscale, 1280 x 1024 pixel resolution at 80 Hz) was used to image from below. The soundproof box with ventilation was illuminated with far-red LEDs. To prevent noise disturbance, doors were kept closed during acquisition. Mice received CNO on day 1, if applicable, and vehicle on day 2 to understand how perturbation may alter open field habituation. Each mouse was recorded for 20 minutes before returning to group housing over two days (first 18 min 46 sec are included in the analysis). Raw images were processed to segment the mouse from the background (median filter) to a final video size of 400 x 400 pixels.

Each frame was aligned for the mouse body axis and body parts were tracked using LEAP (LEAP Estimates Animal Poses) as previously described [1–4,25]. The LEAP network was trained on 1000 frames to find 18 body parts. Automatic classification of animal behavior was performed using custom MATLAB and Python scripts as previously described [29]. Briefly, distances between 11 body parts (nose, chin, 4 x paw tip, 4 x paw base, where paw connects to leg, and tail base) were calculated and the dimensionality was reduced by projecting on the first 10 PCA components. A wavelet analysis was performed in the lower dimensional space, followed by k-means clustering (k = 100) of the frequency data to obtain behavioral clusters. The 100 behavioral clusters were manually grouped into 6 behaviors (slow explore, grooming, fast explore, reared, turning walk, locomotion). A majority filter with a sliding window of 11 frames was used on the predicted behaviors for each frame. Centroid metrics were used to calculate distance traveled, and fraction of time in the inner arena. The inner part of the arena was defined as the region of the arena with a distance larger than 150 pixels (approximately 7.6 cm) to all borders of the arena. The borders were obtained using the space explored by the mouse. To calculate the temporal change of the probability to be in fast locomotion within the time of an experiment, a sliding window of size 20001 frames was used. The probabilities at equally distant time points were calculated for each mouse separately, based on which the mean and standard deviation was obtained (**Figure 2C**).

For the shifts in state occupancy, the fractions of time spent in each behavior during the first five minutes and the remainder of the experiment were calculated for each mouse. Then, the geometric mean was taken for each group and day and the geometric mean values for day 2 were divided by the ones from day 1 for each group (**Figure 2D**). The shifts in state transitions were obtained as follows: First, the transition matrices were calculated for each mouse and day by considering only changes of states as transitions (i.e. the transition rate to stay in the same state is zero). Then, the transition matrices are averaged for each group and day by weighting

the transition probabilities from initial state i by the probability of the mouse to be in state i. Finally, the resulting averaged transition matrix for day 1 is subtracted from the one for day 2 for each group, which allows an investigation of the changes in state transitions across days (**Figure supplement 2E**). To study the possibility of gait changes in cerebellar perturbed mice compared to controls, the phases when the paws enter stance during a single stride of locomotion were calculated for different centroid velocities [41]. The beginning of the stance phase was determined by the peak position of the paw in an animal-centered coordinate system (**Figure supplement 2B**). All analyses of the open field behavioral data were performed using custom Matlab code (https://github.com/PrincetonUniversity/OF-ymaze-cfos-analysis).

Water Y-maze: The water Y-maze assay and analysis was similar to described [15]. Briefly, the Y-shaped transparent polycarbonate apparatus had symmetrical arms, each measuring 33 cm x 7.5 cm x 20.3 cm (length x width x height) from the center. Notches in all three arms (9.5 cm from the center) allowed for a removable gate. A small Pyrex glass container was used as a platform for the mice to climb on. To prevent the animals from seeing the platform, opaque water was used by mixing ACMI certified hypoallergenic non-toxic white paint (Art-Minds, Tempera Paint) in warm water. Water levels were kept at a depth to prevent the animals from touching the bottom of the maze. Between each mouse, excrement was removed and water was exchanged to maintain ideal water temperature between 22-28 degrees Celsius. At the end of the day, water was removed for cleaning by PREempt disinfectant wipes (0.5% Hydrogen Peroxide) and sprayed down with 70% ethanol to be left overnight to dry. To prevent distraction, a three-walled shield was placed around the maze constructed of non-reflective black plastic (34 x 29 x 22 cm, length x width x height). Directly above the arena, a camera (PlayStation Eye) was mounted on a T-slotted aluminum rail (80/20 KNOTTS Company, Berkeley Heights, NJ) and used to record the entire field of view at 50 frames/s using a custom Python 2.7.6 script (Anaconda 1.8.0) and a CLEye Driver (https://codelaboratories.com/products/eye/driver/).

Over four consecutive days animals were habituated to the arena (Day 1; three 60 s trials), learned to find a platform through trial and error (Acquisition Day 2 and Day 3; four sessions with five 40 s trials), then exposed to reversal whereby the platform was moved to the opposite arm the animals learned (Day 4; five sessions with five 40 s trials) (**Figure 3A)**. Mice were required to have 80% success rate for acquisition day 3 in order to progress to the reversal day. During the reversal day, animals were exposed to four sessions of five consecutive trials followed by a fifth forced session whereby a door was placed in the initial learned arm of the maze which no longer has a platform. All mice were kept in a clean cage on a heating pad to dry before returning to their homecage. As the temperature difference between the warming cage and the water can be drastic, it is critical to allow for the animal to cool down prior to starting a new session. Performance on first-choice turn direction in the Y-maze assay was calculated automatically. Distance traveled during habituation was calculated to assess possible muscle damage during surgery (**Figure supplement 4A-C**). Subsequent tries were recorded to calculate the fraction of choices required to reach the platform (**Figure 3D; Figure supplement 4F**).

*Whole-Brain Imaging*

All brains were analyzed and processed similar to Pisano et al., 2021 [1–4,25]. Briefly, cleared brains were glued (Loctite, 234796) ventral-side-down to a 3D printed holder and imaged in DBE. Brains were registered using the autofluorescence channel (488 nm laser diode excitation and 525 emission) to the Princeton Mouse Atlas. Cellular imaging of c-Fos and mCherry expression was acquired using 640 nm excitation and 680 nm emission (1x magnification, 1.3x objective, 0.1 numerical aperture, 9.0 mm working distance, 12.0 x 12.0 mm field of view, LVMI-Fluor 1.3x, LaVision Biotech) with a 10 µm step-size using a 0.016 excitation NA. Analysis of whole-brain c-Fos was completed using ClearMap [34] on high performance computing clusters.

To confirm ClearMap cell counts, two human annotators analyzed 14 brain volumes and found 96.72% correspondence between cells counted by the human annotators and ClearMap counted cells. Structures less than 80 microns and structures in the medulla were removed from analysis. The medulla was not analyzed as it can be damaged during brain extraction. Ventricles, brain edge, and zones within 60 microns of region boundaries were removed. The cerebellum was not analyzed for c-Fos activity. Visualization of brain volumes and cell detections from ClearMap was performed using Neuroglancer. Tissue image processing and registration was performed using custom Python code (https://github.com/PrincetonUniversity/BrainPipe).

We assessed the impact of varying experimental conditions in the following contrasts:

1. Acquisition day 1 vs Habituation
2. CNO control reversal vs CNO control no reversal
3. CNO control reversal vs Vehicle control reversal
4. Vector control reversal vs Vehicle control reversal
5. Lobule VI reversal vs CNO control reversal
6. Crus I left vs CNO control reversal
7. Crus I right vs CNO control reversal
8. Bilateral Crus I vs CNO control reversal
9. Lobule VI reversal vs Lobule VI no reversal

In contrasts 1-5, both the control and the treatment groups of mice were processed in the same batch so as to minimize batch effects. In contrasts 6-7, both control and treatment groups were present in multiple batches, so batch (encoded as a categorical indicator variable) was included as a covariate to adjust for the batch effect. Finally, in contrasts 8-9 control and treatment groups did not overlap within any single batch, impeding the direct adjustment for confounding due to batch effects. However, we were able to adjust for confounding indirectly by using a "bridge variable" strategy. A bridge variable is an experimental group found in both the batch containing treatment animals as well as the batch containing control animals. The bridge variables were Lobule VI reversal  for contrast 8 and CNO control reversal for contrast 9.

Inclusion of the bridge variable along with the batch indicator variables in a regression model makes identification of the treatment versus control contrast statistically identifiable separate from the batch effect.

Each mouse was treated as a single observation or biological replica, consisting of its experimental condition (i.e. treatment or control) and a multivariate outcome of counts of active neurons in each of the brain regions. Total counts of active neurons were highly variable between animals even in the same experimental condition. We therefore sought to explain differences in proportion of total counts for each brain region. Given the overdispersed, discrete nature of the data, we used a negative binomial likelihood and performed separate regressions for each brain region and contrast, using the natural log of total counts as an offset. Specifically, for a given contrast, let $X_i$=1 if animal i is in the treatment group and $X_i$=0 otherwise. Let $Z_i$=1 if animal is in the first batch and $Z_i$=0 otherwise. Let $A_i$=1 if the animal has the bridge variable condition and $A_i$=0 otherwise.Let $T_i$ be the total c-Fos counts across all regions in brain i. Let $Y_{ij}$ be the c-Fos count in region j of brain i. The statistical model is then given by

$$Y_{ij} \sim \text{negative binomial } (\mu_{ij}, \varphi_j)$$

$$\log(\mu_{ij}) = \beta_{0j} + X_i * \beta_{1j} + \ln(T_i) + Z_i * \beta_{2j} + A_i * \beta_{3j}$$

where $\mu_{ij}$ is the expected value of $Y_{ij}$, $\varphi_j$ is the nuisance shape parameter of the negative binomial distribution, and $\beta_{0j}$ is an intercept term which captures the fact that some brain regions have a consistently higher or lower activity level across all animals without regard to their experimental condition (for example this could be because some regions have a larger volume than others).

The parameter $\beta_{1j}$ is of greatest biological interest. It is interpreted as the average change in proportion of c-Fos activity for region j in the treatment group relative to the control group on the logarithmic scale. For example, if $\beta_{1j}$=1.5, the average c-Fos activity for brain

region j is estimated to be exp(1.5)=4.48 times higher in the treatment condition compared to the control condition. If $\beta_{1j}$= -0.7 (a negative coefficient) average c-Fos activity for brain region j is estimated to be exp(-0.7)=0.5 times lower in the treatment condition compared to the control (ie, the treatment mean is half that of the control mean).

We fit each negative binomial regression using the R package MASS [75]. In addition to maximum likelihood estimates of the regression coefficients such as $\beta_{1j}$, this package also computes a standard error for each coefficient. From these we obtained effect sizes in the form of Wald z-test statistics (estimated coefficient divided by standard error). Under the null hypothesis that there is no change in the average c-Fos expression between the treatment and control groups (i.e. $\beta_{1j}$=0), the effect sizes would be expected to follow an asymptotically standard normal distribution. By comparing the computed effect sizes against this null distribution, we obtained p-values. If the p-value was small for a given brain region, it suggested that there was a large difference between the treatment and control groups and the null hypothesis should be rejected for that region. Since a separate statistical test was performed for each brain region, we adjusted raw p-values in each analysis to control the multiple testing false discovery rate (FDR) using the method of Benjamini and Hochberg [76].

In rare cases, numerical errors occurred in the MASS package fitting procedure. This is because estimation of the negative binomial parameters ($\beta_{0j}$, $\beta_{1j}$, $\beta_{2j}$, $\beta_{3j}$, and $\varphi_j$) requires an iterative optimization that can fail to converge. We determined that in most of these cases, the brain region was small and/or irregularly shaped. We therefore dropped such regions from subsequent analysis.

In contrast 8 only, some observations came from batch 201810_adultacutePC_ymaze_cfos, in which brains had cerebellum excised. As a quality control step, we excluded regions with extremely low counts and low variability across all brains in this batch since this would destabilize the regression fitting procedure. Specifically, for each

region we counted the number of brains within the batch having a nonzero count value. If the number of nonzero counts was less than two, we excluded the region.

In addition to analyzing individual brain regions, we also fit negative binomial regressions to examine the effects of experimental perturbations on three composite regions consisting of multiple subregions from our original 122: thalamus, sensory/motor, and polymodal association. For each composite region and experimental contrast, we summed the raw c-Fos cell counts of all constituent subregions within each animal. We then fit negative binomial regressions as previously described, with the natural log of the total counts in the entire brain again used as an offset for each animal. This maintained consistency in the interpretation of the regression coefficients and effect sizes by keeping them on the same (proportional) scale as the original analysis. To confirm our c-Fos statistical results, we ran two sample t-tests for each region per condition comparison, and then checked the validity of the resulting p-values using permutation testing. None of the highly significant regions from the negative binomial regression were missing.

*Acute brain slice experiments*

Mice (C57BL/6J) were prepared as described previously in “Animal preparation” for inhibitory DREADD induction of Purkinje cells at 3-weeks of age. Two weeks later, mice were deeply anesthetized with Euthasol (0.06 ml/30g), decapitated, and the brain removed. The isolated whole brains were immersed in ice-cold carbogenated NMDG ACSF solution (92 mM N-methyl D-glucamine, 2.5 mM KCl, 1.25 mM $NaH_2PO_4$, 30 mM $NaHCO_3$, 20 mM HEPES, 25 mM glucose, 2 mM thiourea, 5 mM Na-ascorbate, 3 mM Na-pyruvate, 0.5 mM $CaCl_2$, 10 mM $MgSO_4$, and 12 mM N-acetyl-L-cysteine, pH adjusted to 7.3–7.4). Parasagittal cerebellar brain slices (270 µm) were cut using a vibratome (VT1200s, Leica Microsystems, Wetzlar, Germany), incubated in NMDG ACSF at 34°C for 15 minutes, and transferred into a holding solution of

HEPES ACSF (92 mM NaCl, 2.5 mM KCl, 1.25 mM $NaH_2PO_4$, 30 mM $NaHCO_3$, 20 mM HEPES, 25 mM glucose, 2 mM thiourea, 5 mM Na-ascorbate, 3 mM Na-pyruvate, 2 mM $CaCl_2$, 2 mM $MgSO_4$ and 12 mM N-acetyl-L-cysteine, bubbled at room temperature with 95% $O_2$ and 5% $CO_2$). During recordings, slices were perfused at a flow rate of 4–5 ml/min with a recording ACSF solution (120 mM NaCl, 3.5 mM KCl, 1.25 mM $NaH_2PO_4$, 26 mM $NaHCO_3$, 1.3 mM $MgCl_2$, 2 mM $CaCl_2$ and 11 mM D-glucose) and continuously bubbled with 95% $O_2$ and 5% $CO_2$.

Whole-cell recordings were performed using a Multiclamp 700B (Molecular Devices, Sunnyvale, CA) using pipettes with a resistance of 3–5 MΩ filled with a potassium-based internal solution (120 mM potassium gluconate, 0.2 mM EGTA, 10 mM HEPES, 5 mM NaCl, 1 mM $MgCl_2$, 2 mM Mg-ATP and 0.3 mM Na-GTP, pH adjusted to 7.2 with KOH). Purkinje neurons expressing mCherry were selected for recordings.

*Statistics*

All statistics were performed using MATLAB, R (rstatix, compositions, npmv, data.table, plyr, ggplot2, ggpubr, car, DescTools), or Python 2 and Python 3 (statsmodels, scipy, matplotlib, numpy). Data are presented as mean ± SD, unless otherwise stated. Group mean comparisons were performed through repeated measures ANOVA (open field) or through one-way ANOVAs with Tukey HSD or Dunnett multiple comparisons post-hoc tests. For each comparison the effect size (Cohen's *d*) or Kolmogorov-Smirnov test was calculated. Normality was tested using the Shapiro-Wilk test, and the homogeneity of variances was tested using Levene's test to determine parametric or nonparametric analysis. If the Shapiro-Wilk test or the Levene's test was significant, the nonparametric Kruskal-Wallis test was performed, followed by pairwise comparisons with Wilcoxon rank sum exact tests (with Benjamini-Hochberg multiple comparison correction). In this case, the Wilcoxon effect size r was calculated for each comparison.

Y-maze performance was measured by the number of successes and failures of each

mouse in 5 trials for different sessions and days. To account for the fact that the data were nested and can take only values between 0 and 100% (more specifically 0, 20, 40, 60, 80 and 100%), we fit generalized mixed effect models (GLMM) with a binomial distribution and logit link function to the performance data for acquisition day 2, 3 and reversal day (using glmer function in R package lme4, [77]. We included the session and the experimental group as fixed effects predictors. Since the performance scores within mice may be correlated, we also incorporated random intercepts in the model. We tested different models (with and without the interaction term of group and session; considering session as a factor or a quantitative variable; with and without random slopes added to random intercepts) and chose the models based on the Akaike information criterion (AIC) and likelihood ratio tests. The data for acquisition day 2 and day 3 was best described by a model without the interaction term of group and session and random intercepts only. To test for significant differences of the performance of the experimental groups, we performed multiple comparisons of the means (Dunnett contrasts) (using the glht function in the R package multcomp, [78]. For the reversal day, we also considered a model that accounts for interactions of group and session and tested for within session differences between the groups (Bonferroni-Holm multiple comparison correction).

The number of structures used for c-Fos analysis were tested for multiple comparisons by calculating the false discovery rate, the coefficient of variation, and by performing permutation tests on each comparison. All c-Fos data is presented as $p<0.01$ unless otherwise stated. To analyze correlations between whole-brain c-Fos/DREADD and behavior, Spearman's rank correlation coefficient ($\rho$) and p-values were determined using stats models in Python 3.

To investigate differences between the behaviors of mice in the open field we performed a compositional data analysis to account for the compositional nature of the data [79]. First, for each mouse, the set of fractions of time spent in each behavior were transformed into isometric log ratio coordinates using the R package ‘compositions’. In this coordinate space, differences between groups were analyzed using a nonparametric multivariate test (Wilks’ Lambda type test

statistics) from the R package 'npmv'. To identify the behaviors that differ between groups, we calculated the bootstrapped 95% confidence intervals (N=5000) of the log ratio differences between the cerebellar perturbed groups and mice without a cerebellar perturbation given CNO on day 1 for each behavior [79]. The same compositional data analysis was performed on the different control groups using the geometric mean values of all control groups combined as a reference group. The Matlab and R code used for the statistical analyses is published on Github (https://github.com/PrincetonUniversity/OF-ymaze-cfos-analysis).

**Supplemental Videos**

**Video S1. Semi-supervised behavioral classification.** Example movie of mouse in open field (left), zoomed-in version with LEAP labels (middle) and corresponding ethogram (right).

**Video S2. Y-maze task.** Example movie of mouse performing Y-maze acquisition, reversal with CNO only, and lobule VI perturbed mouse attempting reversal.

**Video S3. Whole brain lightsheet.** Example movie of a cleared brain using iDISCO+, c-Fos staining, clearmap cell counts, and neuroglancer overlay of multiple thalamic regions.

**Table S1. Effects of experimental perturbations on c-Fos cell counts.** Contrasts include acquisition versus habituation, reversal learning versus acquisition, and lobule VI perturbation via DREADDs against CNO only. For each brain region and contrast, negative binomial (NB) regression was performed with natural log of total counts across all regions as an offset. Estimate: NB slope coefficient for effect of treatment (log-ratio scale), Fold change: exponentiated coefficient (ratio scale), Std. Error: standard error of estimate, z value: estimate divided by standard error (also known as effect size), Pr(>|z|): raw p-value for effect, fdr_adj_pval: p-value adjusted for false discovery rate, status: whether NB fitting routine

encountered numerical problems.

**Acknowledgements:**

We thank Henk-Jan Boele, Ben Deverett, Esteban Engel, Laura Lynch, Christina Matl, Dafina Pacuku, Tiffany Pham, and Fred Uquillas for collaboration and discussion, Greg Horwitz for the L7 plasmid, and Archit Verma and Barbara Engelhardt for discussions on statistical testing. This work was supported by NIH R01 RS045193 and R01 MH115750 (S.W.) and the New Jersey Brain Injury Research Council (J.V.).

**Author Contributions:**

J.V., T.P., M.K., J.S., and S.W. conceived and designed studies. J.V. and C.J. performed viral injections and ran behavior. J.V. prepared tissue, collected images, and performed image analysis. J.V., S.B., M.K., Z.D., A.H., F.W.T., U.K., K.S., J.S., and S.W. performed data analysis and curation. J.V. and S.B. prepared figures. A.H., T.P., F.W.T., and Z.D. designed image analysis algorithms for c-Fos and injection site recovery. U.K., M.K., and S.B. designed methods, analysis and performed statistics for open field analysis. J.L. performed electrophysiology for virus validation. J.V., S.B., and S.W. wrote the initial draft of the manuscript. All authors edited the manuscript.

**Competing interests**

The authors declare that they have no competing interests.

## FIGURES

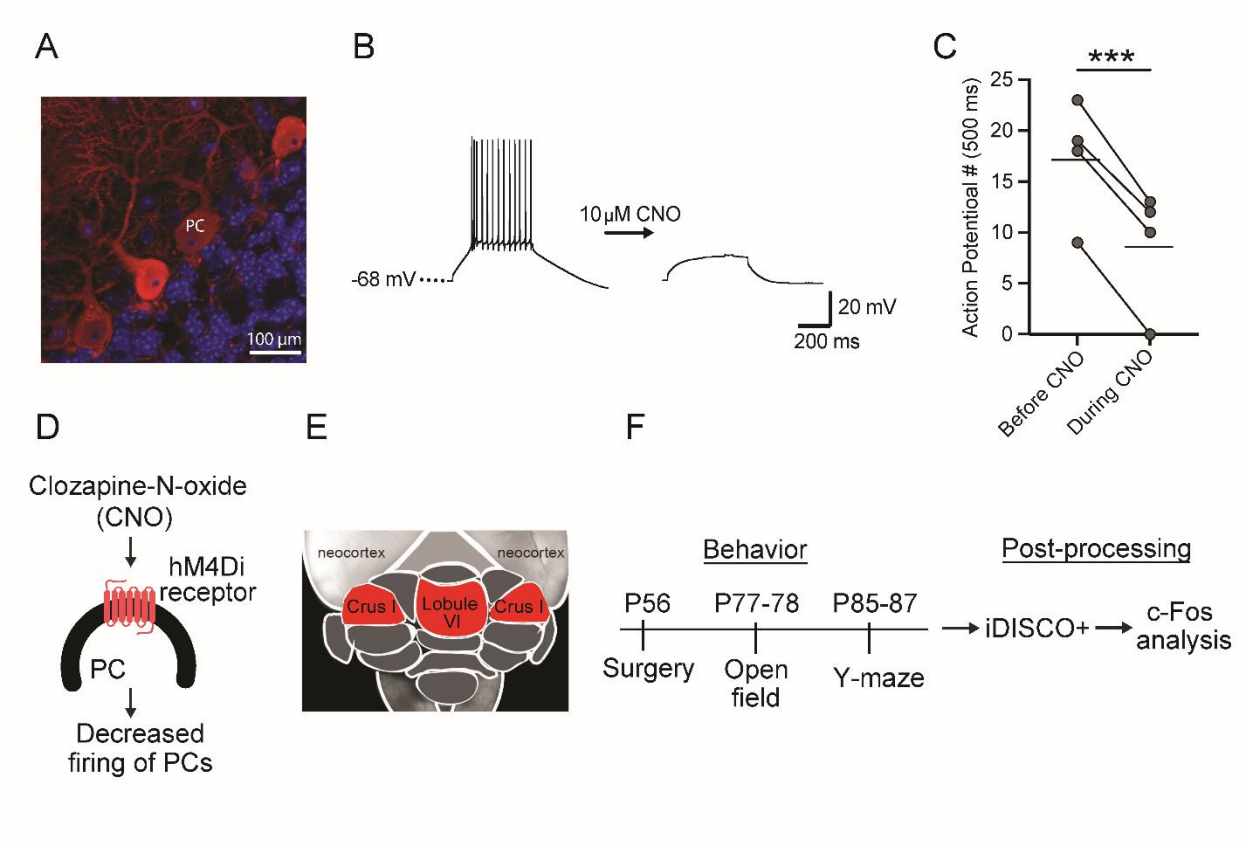


**Figure 1. Acute adult inactivation of Purkinje cells in lobule VI and crus I.** (A) Expression of the chemogenetic DREADD probe in Purkinje cells (red). (B) Slice electrophysiology of Purkinje cells before and during clozapine-N-oxide (CNO; 10 µM). (C) Purkinje cells with DREADD receptors fire fewer action potentials in response to current injection. (D) The activating ligand CNO binds to the hM4Di receptor and decreases firing of Purkinje cells. (E) Dorsal view of cerebellum with targeted lobule VI or crus I indicated in red. (F) Adult mice received surgery for viral AAV injection (DREADDs or mCherry) at P56 for behavioral testing starting with open field between P77-78 and water Y-maze starting between P85-87. For each behavior test, animals received CNO (i.p.), vehicle, or no treatment 20 minutes prior to testing. After behavioral testing, brains were cleared for light-sheet microscopy using iDISCO+ and analysis of c-Fos immunopositive cells. Comparisons were made using a paired t-test. *** $p < 0.001$

| Group | DREADDs | CNO | Open Field | Y-maze |
|---|---|---|---|---|
| Untreated | no | no | 0 | 51 |
| Vehicle only | no | no | 9 | 9 |
| CNO only | no | yes | 12 | 18, 7: no reversal |
| mCherry | no | yes | 10 | 17 |
| Lobule VI | yes | yes | 10 | 10, 10: no reversal |
| Crus I bilateral | yes | yes | 10 | 7 |
| Crus I right | yes | yes | 10 | 25 |
| Crus I left | yes | yes | 10 | 26 |

**Table 1: Experimental groups denoting DREADD and CNO conditions.** Animals underwent surgery for an injection of DREADD or mCherry viral expression. Prior to open field and the water Y-maze task, animals were injected with the DREADD ligand (CNO), Vehicle, or remained untreated.

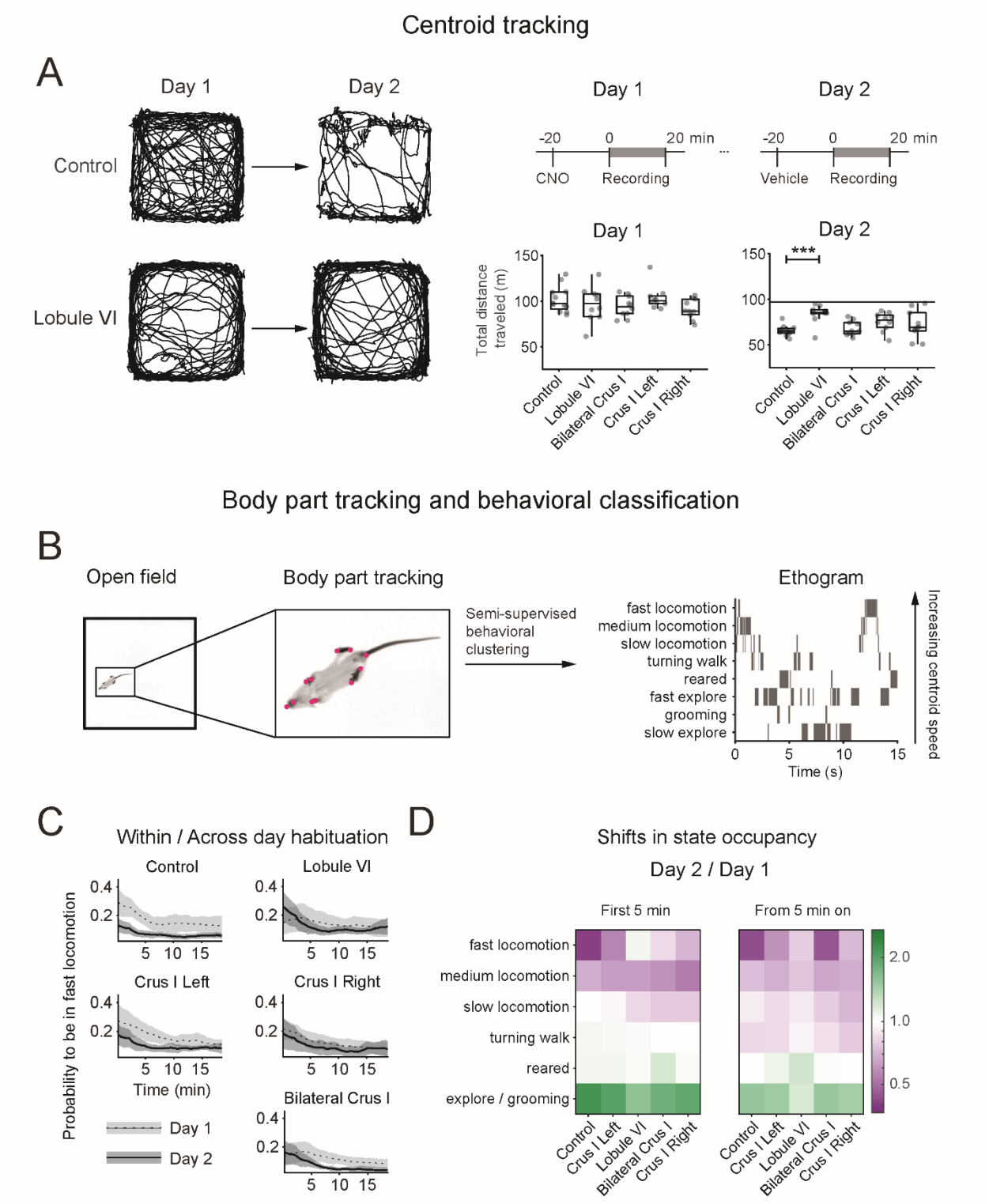


**Figure 2. Effects on spontaneous behavior of perturbation of lobule VI and crus I.** (A) Lobule VI-perturbed mice show a larger total distance travelled on the second day compared to a day-matched no-DREADD control group. Left: Example trajectories of the centroid position of a lobule VI-perturbed mouse and a control mouse in the open field for the first 5 minutes. Top

right: Timeline of the open-field experiments. Comparisons were made using an one-way or two-way mixed ANOVA. (B) Machine learning pipeline to obtain ethograms for the open-field recordings. First, body parts were tracked using LEAP. These postures were then processed as described in Klibaite et al. 2021 to assign one of six behaviors to each time point in the recording. Locomotion was divided into slow, medium and fast based on the centroid velocity of the mouse. (C) The probability to be in the fast locomotion state decreased within and across days for the control group and crus I left, but lobule VI-, bilateral crus I- and crus I right-perturbed mice show a higher or similar probability to be in fast locomotion at the beginning of the experiment on the second day compared to the first day. (D) The state occupancies for lobule VI-perturbed mice changed less across days than the other groups, indicating a lack of adaptation. *** $p < 0.001$

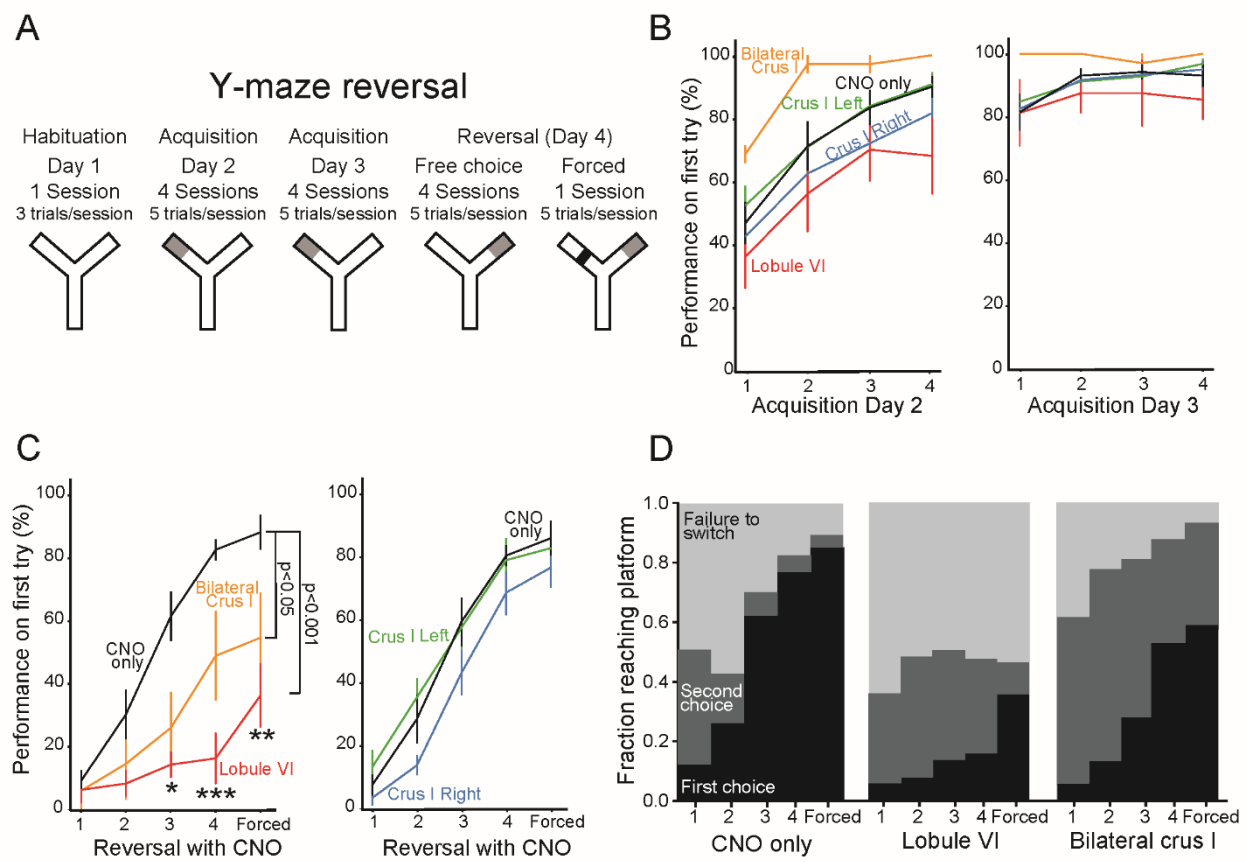


**Figure 3. Effect of lobule VI and crus I inactivation on behavior.** (A) Protocol for Y-maze reversal consisting of habituation, two days of training (day 2 and day 3), and one reversal day ending in a forced session (day 4). (B) Animals learned to find the platform over two days. First try performance of 80% at the end of session 4 was required to continue to reversal. (C) Y-maze reversal was impaired in animals with lobule VI and bilateral crus I (left) inactivation compared to controls. Unilateral effects were not found (right) compared to controls. (D) Normal mice learned through trial and error, demonstrating more accurate performance over time. Lobule VI and crus I perturbed mice stayed repeatedly with the original incorrect choice. Error bars indicate mean ± SEM. Comparisons were made using a generalized mixed effect model (GLMM) with a binomial distribution. * $p < 0.05$, ** $p < 0.01$, *** $p < 0.001$

`

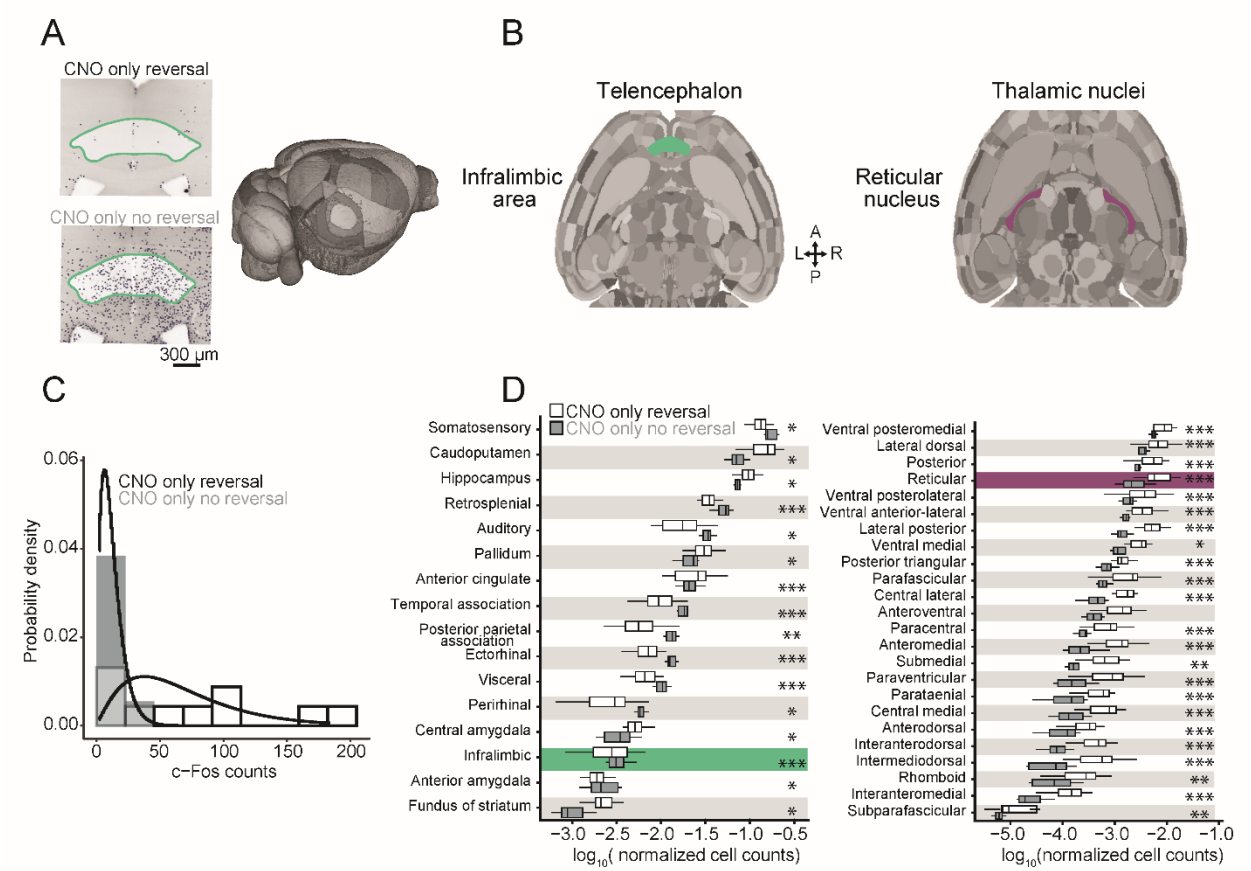


**Figure 4. Whole-brain analysis of c-Fos.** (A) Example of ClearMap cell counting in the infralimbic area (left). Neuroglancer 3-D mouse brain (right). (B) Example horizontal mouse brain sections representing infralimbic area (green) and reticular nucleus (purple). (C) Negative binomial regression under the two experimental condition groups. This example, nucleus raphe pontis. Nonparametric kernel density estimates derived from count-based densities (bars). Solid curves indicate the probabilities at each count level from a fitted negative binomial regression model. (D) Normalized cell counts ($log_{10}$) in the telencephalon (left) and thalamus (right) comparing reversal (white) and no-reversal (gray). Both groups received CNO. Comparisons were made using a negative binomial regression. * $p < 0.05$, ** $p < 0.01$, *** $p < 0.001$

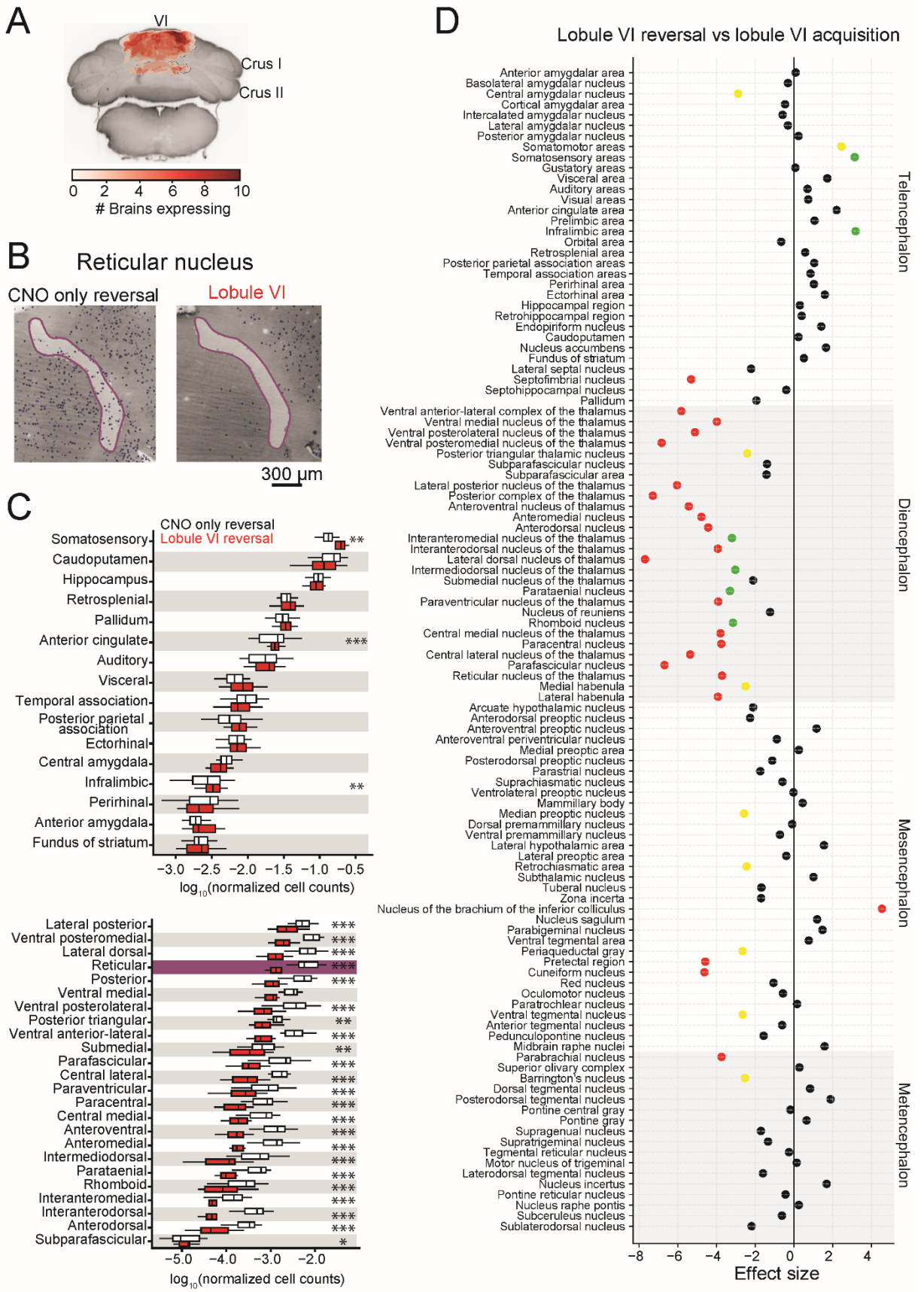

**Figure 5. Effects of Lobule VI perturbation on whole-brain c-Fos.** (A) Overlay of regions of DREADD-AAV expression recovered using immunofluorescent labeling of mCherry and lightsheet microscopy imaging. (B) Example images of ClearMap cell counting in the reticular nucleus. (C) Normalized cell counts ($log_{10}$) by total regions analyzed in the telencephalon (top) and thalamus (bottom). (D) Statistically-significant ($p < 0.05$) lobule VI reversal versus lobule VI acquisition. Lobule VI perturbation modulated regions necessary for reversal learning, including thalamus. Comparisons were made using a negative binomial regression. Yellow: * $p < 0.05$, Green: ** $p < 0.01$, Red: *** $p < 0.001$

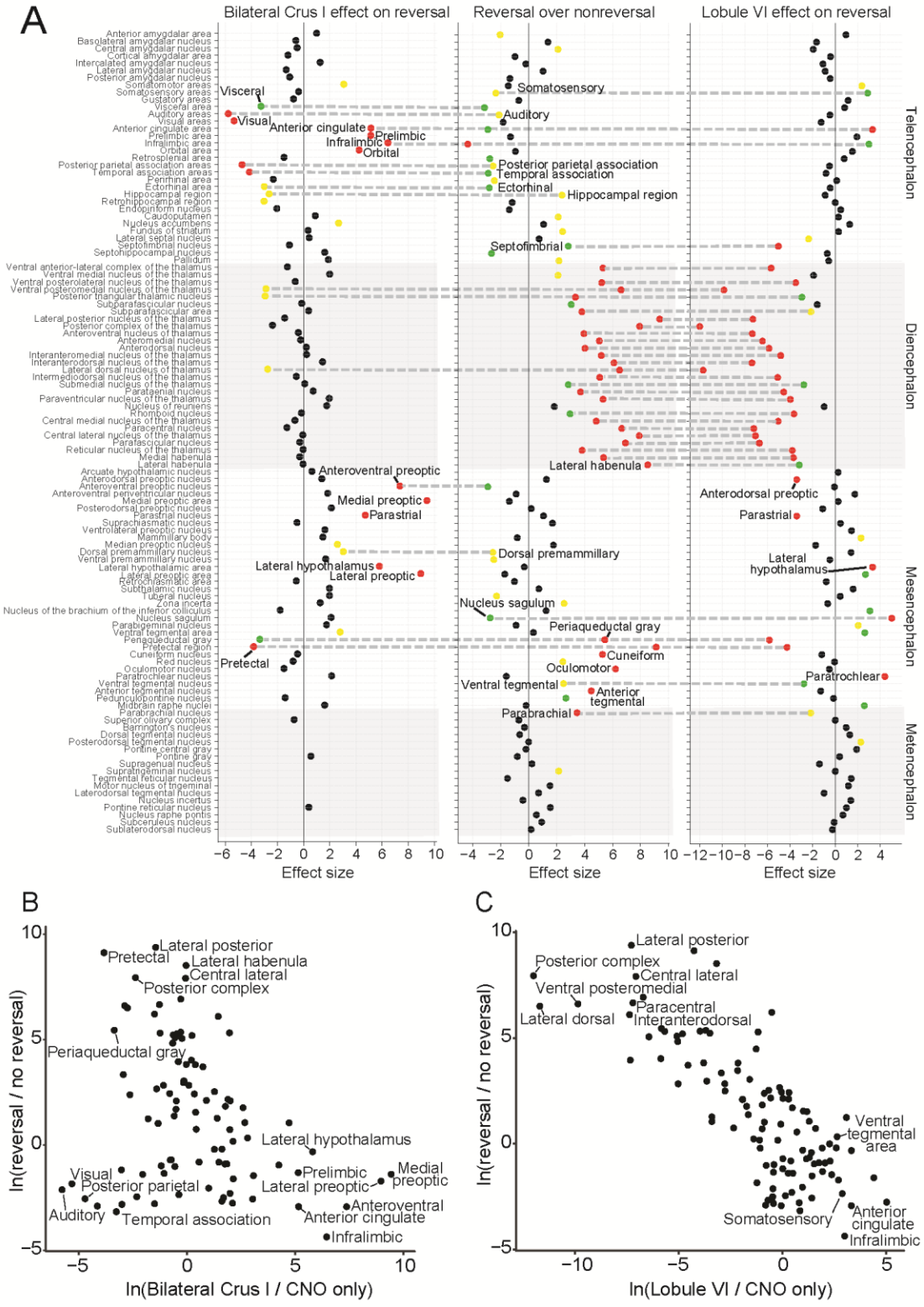

**Figure 6. Brain-wide association study to identify activated regions of c-Fos expression.** (A) Statistically-significant ($p < 0.05$) bilateral crus I (left), reversal (middle) lobule VI (right) structures. Lobule VI (right) perturbation modulated regions necessary for reversal learning, including thalamus and anterior cingulate cortex. Crus I bilateral (left) perturbation altered regions in the telencephalon, including prelimbic, infralimbic, anterior cingulate, and orbital frontal cortex (B) Correlations between crus I and reversal learning structures (Pearson's $r = -0.29$). (C) A strong negative correlation was found between lobule VI and reversal learning structures (Pearson's $r = -0.78$). All data were calculated as the natural log of ratios rescaled by the standard error. Comparisons were made using a negative binomial regression. Yellow: $p < 0.05$, Green: $p < 0.01$, Red: $p < 0.001$

## References


1. Leiner, H. C., Leiner, A. L. & Dow, R. S. Does the cerebellum contribute to mental skills? *Behav. Neurosci.* **100**, 443–454 (1986).
2. Leiner, H. C., Leiner, A. L. & Dow, R. S. Cognitive and language functions of the human cerebellum. *Trends Neurosci.* **16**, 444–447 (1993).
3. De Zeeuw, C. I., Lisberger, S. G. & Raymond, J. L. Publisher Correction: Diversity and dynamism in the cerebellum. *Nat. Neurosci.* **24**, 450 (2021).
4. De Zeeuw, C. I. Bidirectional learning in upbound and downbound microzones of the cerebellum. *Nat. Rev. Neurosci.* **22**, 92–110 (2021).
5. Schmahmann, J. D. & Sherman, J. C. The cerebellar cognitive affective syndrome. *Brain* **121 ( Pt 4)**, 561–579 (1998).
6. Schmahmann, J. D. Cerebellar Cognitive Affective Syndrome and the Neuropsychiatry of the Cerebellum. *Handbook of the Cerebellum and Cerebellar Disorders* 1717–1751 (2013) doi:10.1007/978-94-007-1333-8_77.
7. Limperopoulos, C., Chilingaryan, G., Guizard, N., Robertson, R. L. & Du Plessis, A. J. Cerebellar Injury in the Premature Infant Is Associated With Impaired Growth of Specific Cerebral Regions. *Pediatr. Res.* **68**, 145–150 (2010).
8. Wang, S. S.-H., Kloth, A. D. & Badura, A. The cerebellum, sensitive periods, and autism. *Neuron* **83**, 518–532 (2014).
9. Limperopoulos, C. *et al.* Injury to the premature cerebellum: outcome is related to remote cortical development. *Cereb. Cortex* **24**, 728–736 (2014).
10. Uddin, L. Q. *et al.* Brain State Differentiation and Behavioral Inflexibility in Autism. *Cereb. Cortex* **25**, 4740–4747 (2015).
11. Latinus, M. *et al.* Inflexibility in Autism Spectrum Disorder: Need for certainty and atypical emotion processing share the blame. *Brain Cogn.* **136**, 103599 (2019).
12. Fatemi, S. H. *et al.* Consensus paper: pathological role of the cerebellum in autism. *Cerebellum* **11**, 777–807 (2012).
13. Crucitti, J., Hyde, C., Enticott, P. G. & Stokes, M. A. Are Vermal Lobules VI-VII Smaller in Autism Spectrum Disorder? *Cerebellum* **19**, 617–628 (2020).
14. Traut, N. *et al.* Cerebellar Volume in Autism: Literature Meta-analysis and Analysis of the Autism Brain Imaging Data Exchange Cohort. *Biol. Psychiatry* **83**, 579–588 (2018).
15. Badura, A., Verpeut, J. L., Metzger, J. W. & Pereira, T. D. Normal cognitive and social development require posterior cerebellar activity. *Elife* (2018).
16. Stoodley, C. J. *et al.* Altered cerebellar connectivity in autism and cerebellar-mediated rescue of autism-related behaviors in mice. *Nat. Neurosci.* **20**, 1744–1751 (2017).
17. Deverett, B., Kislin, M., Tank, D. W. & Wang, S. S.-H. Cerebellar disruption impairs working memory during evidence accumulation. *Nat. Commun.* **10**, 3128 (2019).
18. Deverett, B., Koay, S. A., Oostland, M. & Wang, S. S.-H. Cerebellar involvement in an evidence-accumulation decision-making task. *eLife* vol. 7 (2018).
19. Strick, P. L., Dum, R. P. & Fiez, J. A. Cerebellum and nonmotor function. *Annu. Rev. Neurosci.* **32**, 413–434 (2009).
20. Eccles, J. C., Llinás, R. & Sasaki, K. The excitatory synaptic action of climbing fibres on the Purkinje cells of the cerebellum. *J. Physiol.* **182**, 268–296 (1966).
21. Kelly, R. M. & Strick, P. L. Cerebellar loops with motor cortex and prefrontal cortex of a nonhuman primate. *J. Neurosci.* **23**, 8432–8444 (2003).
22. Andersson, G. & Oscarsson, O. Climbing fiber microzones in cerebellar vermis and their projection to different groups of cells in the lateral vestibular nucleus. *Exp. Brain Res.* **32**, 565–579 (1978).
23. Apps, R. & Hawkes, R. Cerebellar cortical organization: a one-map hypothesis. *Nat. Rev. Neurosci.* **10**, 670–681 (2009).

24. Gravel, C. & Hawkes, R. Parasagittal organization of the rat cerebellar cortex: direct comparison of Purkinje cell compartments and the organization of the spinocerebellar projection. *J. Comp. Neurol.* **291**, 79–102 (1990).
25. Pisano, T. J. *et al.* Homologous organization of cerebellar pathways to sensory, motor, and associative forebrain. *Cell Rep.* **36**, 109721 (2021).
26. Sillitoe, R. V., Künzle, H. & Hawkes, R. Zebrin II compartmentation of the cerebellum in a basal insectivore, the Madagascan hedgehog tenrec Echinops telfairi. *J. Anat.* **203**, 283–296 (2003).
27. Reeber, S. L., White, J. J., George-Jones, N. A. & Sillitoe, R. V. Architecture and development of olivocerebellar circuit topography. *Front. Neural Circuits* **6**, 115 (2012).
28. Ozol, K., Hayden, J. M., Oberdick, J. & Hawkes, R. Transverse zones in the vermis of the mouse cerebellum. *J. Comp. Neurol.* **412**, 95–111 (1999).
29. Klibaite, U., Kislin, M., Verpeut, J. L., Sun, X. & Shaevitz, J. W. Deep behavioral phenotyping of mouse autism models using open-field behavior. *bioRxiv* (2021).
30. Pereira, T. D. *et al.* Fast animal pose estimation using deep neural networks. *Nature Methods* **16**, 117–125 (2019).
31. Tsai, P. T. *et al.* Sensitive Periods for Cerebellar-Mediated Autistic-like Behaviors. *Cell Rep.* **25**, 357–367.e4 (2018).
32. Dragunow, M. & Faull, R. The use of c-fos as a metabolic marker in neuronal pathway tracing. *J. Neurosci. Methods* **29**, 261–265 (1989).
33. Renier, N. *et al.* iDISCO: a simple, rapid method to immunolabel large tissue samples for volume imaging. *Cell* **159**, 896–910 (2014).
34. Renier, N. *et al.* Mapping of Brain Activity by Automated Volume Analysis of Immediate Early Genes. *Cell* **165**, 1789–1802 (2016).
35. Burton, H. & Jones, E. G. The posterior thalamic region and its cortical projection in New World and Old World monkeys. *J. Comp. Neurol.* **168**, 249–301 (1976).
36. Jones, E. G. *The Thalamus*. (Springer Science & Business Media, 2012).
37. Wiltschko, A. B. *et al.* Mapping Sub-Second Structure in Mouse Behavior. *Neuron* **88**, 1121–1135 (2015).
38. Wiltschko, A. B. *et al.* Revealing the structure of pharmacobehavioral space through motion sequencing. *Nat. Neurosci.* (2020) doi:10.1038/s41593-020-00706-3.
39. Mathis, A. *et al.* DeepLabCut: markerless pose estimation of user-defined body parts with deep learning. *Nat. Neurosci.* **21**, 1281–1289 (2018).
40. Nath, T. *et al.* Using DeepLabCut for 3D markerless pose estimation across species and behaviors. *Nat. Protoc.* **14**, 2152–2176 (2019).
41. Machado, A. S., Darmohray, D. M., Fayad, J., Marques, H. G. & Carey, M. R. A quantitative framework for whole-body coordination reveals specific deficits in freely walking ataxic mice. *Elife* **4**, (2015).
42. Tsai, P. T. *et al.* Autistic-like behaviour and cerebellar dysfunction in Purkinje cell Tsc1 mutant mice. *Nature* **488**, 647–651 (2012).
43. Maes, J. H. R., Eling, P. A. T. M., Wezenberg, E., Vissers, C. T. W. M. & Kan, C. C. Attentional set shifting in autism spectrum disorder: differentiating between the role of perseveration, learned irrelevance, and novelty processing. *J. Clin. Exp. Neuropsychol.* **33**, 210–217 (2011).
44. Sasson, N. J., Turner-Brown, L. M., Holtzclaw, T. N., Lam, K. S. L. & Bodfish, J. W. Children with autism demonstrate circumscribed attention during passive viewing of complex social and nonsocial picture arrays. *Autism Res.* **1**, 31–42 (2008).
45. Reese, R. M., Richman, D. M., Zarcone, J. & Zarcone, T. Individualizing Functional Assessments for Children with Autism: The Contribution of Perseverative Behavior and Sensory Disturbances to Disruptive Behavior. *Focus Autism Other Dev. Disabl.* **18**, 89–94 (2003).

46. Kelly, E. *et al.* Regulation of autism-relevant behaviors by cerebellar-prefrontal cortical circuits. *Nat. Neurosci.* **23**, 1102–1110 (2020).
47. Caulfield, M. D., Zhu, D. C., McAuley, J. D. & Servatius, R. J. Individual differences in resting-state functional connectivity with the executive network: support for a cerebellar role in anxiety vulnerability. *Brain Struct. Funct.* **221**, 3081–3093 (2016).
48. Ottaviani, C. *et al.* Neurobiological substrates of cognitive rigidity and autonomic inflexibility in generalized anxiety disorder. *Biol. Psychol.* **119**, 31–41 (2016).
49. Schmahmann, J. D. Disorders of the cerebellum: ataxia, dysmetria of thought, and the cerebellar cognitive affective syndrome. *J. Neuropsychiatry Clin. Neurosci.* **16**, 367–378 (2004).
50. Hu, H., Cui, Y. & Yang, Y. Circuits and functions of the lateral habenula in health and in disease. *Nat. Rev. Neurosci.* **21**, 277–295 (2020).
51. Andres, K. H., von Düring, M. & Veh, R. W. Subnuclear organization of the rat habenular complexes. *J. Comp. Neurol.* **407**, 130–150 (1999).
52. Chiang, M. C. *et al.* Parabrachial Complex: A Hub for Pain and Aversion. *J. Neurosci.* **39**, 8225–8230 (2019).
53. Deng, H., Xiao, X. & Wang, Z. Periaqueductal Gray Neuronal Activities Underlie Different Aspects of Defensive Behaviors. *J. Neurosci.* **36**, 7580–7588 (2016).
54. Capuzzo, G. & Floresco, S. B. Prelimbic and Infralimbic Prefrontal Regulation of Active and Inhibitory Avoidance and Reward-Seeking. *J. Neurosci.* **40**, 4773–4787 (2020).
55. Boulougouris, V., Dalley, J. W. & Robbins, T. W. Effects of orbitofrontal, infralimbic and prelimbic cortical lesions on serial spatial reversal learning in the rat. *Behav. Brain Res.* **179**, 219–228 (2007).
56. Ghahremani, D. G., Monterosso, J., Jentsch, J. D., Bilder, R. M. & Poldrack, R. A. Neural components underlying behavioral flexibility in human reversal learning. *Cereb. Cortex* **20**, 1843–1852 (2010).
57. Fujita, H., Kodama, T. & du Lac, S. Modular output circuits of the fastigial nucleus for diverse motor and nonmotor functions of the cerebellar vermis. *Elife* **9**, (2020).
58. Halassa, M. M. & Kastner, S. Thalamic functions in distributed cognitive control. *Nat. Neurosci.* **20**, 1669–1679 (2017).
59. Houser, C. R., Vaughn, J. E., Barber, R. P. & Roberts, E. GABA neurons are the major cell type of the nucleus reticularis thalami. *Brain Res.* **200**, 341–354 (1980).
60. Harting, J. K., Van Lieshout, D. P. & Feig, S. Connectional studies of the primate lateral geniculate nucleus: distribution of axons arising from the thalamic reticular nucleus of Galago crassicaudatus. *J. Comp. Neurol.* **310**, 411–427 (1991).
61. Guillery, R. W. & Harting, J. K. Structure and connections of the thalamic reticular nucleus: Advancing views over half a century. *J. Comp. Neurol.* **463**, 360–371 (2003).
62. Cavdar, S. *et al.* Cerebellar connections to the rostral reticular nucleus of the thalamus in the rat. *J. Anat.* **201**, 485–491 (2002).
63. Saper, C. B. Hypothalamic connections with the cerebral cortex. in *Progress in Brain Research* vol. 126 39–48 (Elsevier, 2000).
64. Vanderwolf, C. H. & Stewart, D. J. Thalamic control of neocortical activation: a critical re-evaluation. *Brain Res. Bull.* **20**, 529–538 (1988).
65. Fuller, P. M., Sherman, D., Pedersen, N. P., Saper, C. B. & Lu, J. Reassessment of the structural basis of the ascending arousal system. *J. Comp. Neurol.* **519**, 933–956 (2011).
66. Fields, R. D., Eshete, F., Stevens, B. & Itoh, K. Action potential-dependent regulation of gene expression: temporal specificity in ca2+, cAMP-responsive element binding proteins, and mitogen-activated protein kinase signaling. *J. Neurosci.* **17**, 7252–7266 (1997).
67. Ozaki, K. *et al.* Functional SNPs in the lymphotoxin-α gene that are associated with susceptibility to myocardial infarction. *Nat. Genet.* **32**, 650–654 (2002).
68. Manvich, D. F. *et al.* The DREADD agonist clozapine N-oxide (CNO) is reverse-

metabolized to clozapine and produces clozapine-like interoceptive stimulus effects in rats and mice. *Sci. Rep.* **8**, 3840 (2018).
69. Gomez, J. L. *et al.* Chemogenetics revealed: DREADD occupancy and activation via converted clozapine. *Science* **357**, 503–507 (2017).
70. Jendryka, M. *et al.* Pharmacokinetic and pharmacodynamic actions of clozapine-N-oxide, clozapine, and compound 21 in DREADD-based chemogenetics in mice. *Sci. Rep.* **9**, 4522 (2019).
71. Kloth, A. D. *et al.* Cerebellar associative sensory learning defects in five mouse autism models. *eLife* vol. 4 (2015).
72. Giovannucci, A. *et al.* Cerebellar granule cells acquire a widespread predictive feedback signal during motor learning. *Nat. Neurosci.* **20**, 727–734 (2017).
73. François, A. *et al.* A Brainstem-Spinal Cord Inhibitory Circuit for Mechanical Pain Modulation by GABA and Enkephalins. *Neuron* **93**, 822–839.e6 (2017).
74. Kwiatkowski, D. J. *et al.* A mouse model of TSC1 reveals sex-dependent lethality from liver hemangiomas, and up-regulation of p70S6 kinase activity in Tsc1 null cells. *Hum. Mol. Genet.* **11**, 525–534 (2002).
75. Venables, W. N. & Ripley, B. D. Modern Applied Statistics with S. *Statistics and Computing* (2002) doi:10.1007/978-0-387-21706-2.
76. Benjamini, Y. & Hochberg, Y. Controlling the false discovery rate: A practical and powerful approach to multiple testing. *J. R. Stat. Soc.* **57**, 289–300 (1995).
77. Bates, D., Mächler, M., Bolker, B. & Walker, S. Fitting Linear Mixed-Effects Models Using lme4. *Journal of Statistical Software, Articles* **67**, 1–48 (2015).
78. Hothorn, T., Bretz, F. & Westfall, P. Simultaneous inference in general parametric models. *Biom. J.* **50**, 346–363 (2008).
79. Martín Fernández, J. A., Daunis i Estadella, J. & Mateu i Figueras, G. On the interpretation of differences between groups for compositional data. *SORT: statistics and operations research transactions, 2015, vol. 39, núm. 2, p. 231-252* (2015).